What Controls Dynamics of Droplet Shape Evolution upon Impingement on a Solid Surface?

Wenchao Zhou, Drew Loney, F. Levent Degertekin, and David W. Rosen
The G.W. Woodruff School of Mechanical Engineering, Georgia Institute of Technology, Atlanta, GA 30332

Andrei G. Fedorov
The G.W. Woodruff School of Mechanical Engineering, Georgia Institute of Technology, Atlanta, GA 30332

Parker H. Petit Institute of Bioengineering and Bioscience, Georgia Institute of Technology, Atlanta, GA 30332

DOI 10.1002/aic.14050
Published online February 27, 2013 in Wiley Online Library (wileyonlinelibrary.com)

A shape coefficient is introduced to quantify droplet shape by measuring its similarity to a desired shape to enable the study of droplet shape evolution upon impingement on a solid surface. Parametric simulations are performed with an experimentally validated numerical model to determine the impact conditions to maximize the shape coefficient. Results show that the Weber number is the controlling factor that determines the maximum achievable shape coefficient and the time instant when it is achieved for small Ohnesorge numbers, whereas the Reynolds number becomes the key parameter defining the optimal shape when the Ohnesorge number is large. A regime map is also developed to define the regions where a desired droplet shape can be achieved without splash. © 2013 American Institute of Chemical Engineers *AIChE J*, 59: 3071–3082, 2013
Keywords: droplet impact, shape evolution, shape coefficient

Introduction

Droplet impact on a solid surface has been fascinating to scientists due to its natural beauty in many natural phenomena, as well as its importance to many industrial applications. However, the complicated physics behind the stunning photographs of droplet impact have been puzzling for over a century since Worthington first studied it in 1876.[1] Much research has been conducted and significant progress has been reported during the past century.[2] Chandra and Avedisian[3] studied the collision of a liquid droplet on a solid metallic surface with greatly improved quality of images. Zhao et al.[4] recorded the splat radius during spreading and recoiling on a flat surface with refined time resolution. Kim and Chun[5] have performed experimental study on the spreading and recoiling of different droplets on different solid surfaces. Šikalo et al.[6] studied the droplets impact on inclined surfaces. Perelaer et al.[7] investigated the impact of droplets with various molar mass on a dry solid surface. Son et al.[8] performed study on the spreading of a droplet on a solid surface with a controlled contact angle. Léopoldès et al.[9] studied the droplet impact on chemically heterogeneous surfaces. Experimental studies have also been performed on time evolution of droplet spreading radius on a solid surface.[10] A regime map has been constructed to characterize different modes of spreading dynamics based on the combination of driving forces and resistances.[11] The fluid dynamics at the contact line has also been extensively studied to unravel its complexity. The contact angle hysteresis phenomenon has first been observed and reported by Dussan.[12] A later study showed that surface inhomogeneity, surface roughness, and impurities on the surface could all contribute to the contact angle hysteresis.[13] The contact angle change with temperature has been studied by different research groups.[3,14,15] Splash phenomena are of considerable interest. An empirical dimensionless number has been proposed experimentally to indicate the threshold for splash.[16,17] Three factors have been identified for causing splash: the surrounding gas,[18,19] the surface roughness,[16,19,20] and the compliance of the solid substrate.[21]

Analytical modeling of droplet impact has been difficult due to the complicated physics and nonlinear nature of the governing different equations. The simplified one-dimensional (1-D) models have been proposed by only considering one parameter (the wetted area or the droplet spreading radius). Frenkel first derived the form of a spreading droplet using variational method.[22] Bechtel et al.[23] included the change in kinetic energy in a variational approach in 1981, and many different kinds of 1-D models have been proposed since then[3,14,22,24–26] to describe different impact conditions by approximating the drop shape with spherical cap, cylinder or rimmed cylinder shapes.[27] Numerical simulations have been an important alternative to study droplet impact dynamics. The challenge of numerical modeling of droplet impact arises from the moving interface between the droplet and the surrounding gas, which is difficult in terms of both physical modeling and numerical implementation. Many different numerical models have been proposed based on Navier–Stokes equations, such as marker-and-cell method by Harlow and Welch,[28] volume of fluid (VOF) method, level-set method,[29] front-tracking method,[30] phase-field method,[31] and so forth. Bussmann et al.[32] also developed a 3-D model based on the VOF method to study droplet impact on an inclined surface. Schwartz and Eley[33] simulated droplet motion on low energy and heterogeneous surfaces. A numerical model using the

Correspondence concerning this article should be addressed to W. Zhou at wzhou37@gatech.edu.

Lattice Boltzmann method has also been developed to study droplet impact.[34]

However, most of the previous research focused on studying droplet spreading radius or similar metrics. Little attention has been paid to the change of droplet shape and its relationship to the physics of droplet impact, which is often more important to control for a wide range of industrial applications than just the droplet spreading radius. For instance, if one wants to build a uniform film with inkjet printing for thin film deposition, it would be important to know how close one can make a single-droplet shape resemble a uniform film (i.e., a pancake-like shape) upon impingement on the substrate. Since uniform film deposition and uniform coating are of great industrial interests, this article presents a comprehensive theoretical investigation of the droplet shape change during the impact focusing on how to flatten a single droplet (i.e., to form a pancake-like film) without splash under different impact conditions, which is essential for achieving a desired quality of coatings in ink-jet deposition, thermal spraying, and so forth. An integral metric is proposed to characterize the droplet shape by measuring the similarity between the achieved droplet shape and a desired pancake-like shape. Compared with conventional metrics such as the spread factor,[10] the proposed shape coefficient can capture more details of the droplet spreading and it contains important information about the similarity of the droplet shape to a desired shape that is very important for a number of industrial applications. In addition, this shape metric can be qualitatively related to the physical forces of droplet spreading and, thus, provides a method to investigate the physics of droplet shape evolution. Simulations are used to identify the conditions in terms of relevant dimensionless numbers for achieving a desired shape and at what stage (time instant) of the impact dynamics.

The rest of the article is organized as follows. First, a theoretical model for droplet impact along with its numerical implementation and validation is presented. A metric of droplet shape characterization is defined and the reasoning behind the definition is provided in the next section. Then, a series of simulations are conducted to study the droplet shape evolution and results are discussed. The following section presents a regime map for finding the hydrodynamic conditions that would yield a desired droplet flattening upon impact without splash. Conclusions are given in the last section.

Numerical Model and Validation

Numerical modeling

We start our modeling with several assumptions to simplify the analysis for the impact conditions of interest. First, the fluid is assumed to be incompressible because the impact velocities of interest are much lower than the speed of sound. The shape of the droplet is assumed to be spherical prior to impact. The fluid flow is assumed to be Newtonian, both liquid and gas flow are treated as laminar, and the viscosity and surface tension are assumed to be constant during the impact. The droplet and substrate are assumed to be isothermal.

With the assumptions above, the equations of mass and momentum conservation are as follows

$$\nabla \cdot \mathbf{u} = 0 \tag{1}$$

$$\rho \frac{\partial \mathbf{u}}{\partial t} + \rho \mathbf{u} \cdot \nabla \mathbf{u} = \nabla \cdot \left[-p\mathbf{I} + \eta \left(\nabla \mathbf{u} + (\nabla \mathbf{u})^T \right) \right] + \mathbf{F} \tag{2}$$

where ρ is the fluid's density (kg/m^3), $\mathbf{u}$ is the velocity vector (m/s), p is the pressure (Pa), η denotes the dynamic viscosity (Pa·s), $\mathbf{F}$ is the body force, and $\mathbf{I}$ is the identity matrix.

The phase-field method[31] is adopted to track the movement and deformation of the interface between the liquid phase and gas phase on a fixed grid. Unlike the sharp interface models, such as VOF, level-set, and so forth, the phase-field method provides a way of modeling interfacial forces as continuum forces by treating the interface as a diffusive interface described by the Cahn–Hilliard equation,[35] which ensures the correct dissipation of energy.

The commercially available software COMSOL 3.5a is used to implement the model. COMSOL introduces a phase-field variable ϕ to represent different phases instead of using the composition variable C that ranges from 0 to 1. The phase-field variable ϕ is taken to be $(2C-1)$ and, thus, ranges from -1 to 1, with -1 in the gas phase, 1 in the liquid phase, and -1 to 1 across the interface. The convective Cahn–Hilliard equation describes the evolution of the interface in terms of the phase-field variable

$$\frac{\partial \phi}{\partial t} + (\mathbf{u} \cdot \nabla)\phi = \nabla \cdot (M \nabla \mu) \tag{3}$$

where M is the mobility (m^{3}s/kg) and μ is the chemical potential (Pa) of both phases.

To compute the chemical potential, the mixing energy needs to be defined following the Ginzburg–Landau form[36]

$$E_{mix}(\phi, \nabla\phi) = \frac{\lambda}{4\varepsilon^2}\left(\phi^2 - 1\right)^2 + \frac{\lambda}{2}|\nabla\phi|^2 \tag{4}$$

where λ is the mixing energy density (N) and ε is the interface thickness (m), which are related by[36]

$$\sigma = \frac{2\sqrt{2}}{3}\frac{\lambda}{\varepsilon} \tag{5}$$

where σ is the surface tension between liquid and the surrounding gas. Therefore, the chemical potential can be obtained by[31]

$$\mu = \frac{\partial E_{mix}}{\partial \phi} - \nabla \cdot \frac{\partial E_{mix}}{\partial \nabla \phi} = \lambda\left(-\nabla^2\phi + \frac{\phi\left(\phi^2 - 1\right)}{\varepsilon^2} \right) \tag{6}$$

When the interface thickness ε approaches 0, the asymptotic limit of the phase-field model is the sharp interface model. In this limit, the mobility M and the interface thickness ε must reduce to 0 at the same time. Thus, a constraint is placed on M and ε

$$M = \alpha\varepsilon^2 \tag{7}$$

where α is a tuning parameter.

Unlike the sharp interface models that have to deal with the discontinuities across the interface to calculate the interfacial force due to surface tension, a continuum body force $\mathbf{F_{st}}$ is used in the phase-field model to include the effect of surface tension within the diffusive interface domain, which is calculated by

$$\mathbf{F}_{st} = \mu \nabla \phi \tag{8}$$

Taking into account the gravity force $\mathbf{F_g}$, the total body force $\mathbf{F}$ in Eq. 2 becomes

$$\mathbf{F} = \mathbf{F}_g + \mathbf{F}_{st} = \rho\mathbf{g} + \mu\nabla\phi \tag{9}$$

where $\mathbf{g}$ is the gravity vector.

The governing equations are nondimensionalized based on the following scaling

$$\mathbf{x}^*=\frac{\mathbf{x}}{L};\mathbf{u}^*=\frac{\mathbf{u}}{U};t^*=\frac{tU}{L};p^*=\frac{p}{\rho_{ref}U^2};\mathbf{g}^*=\frac{\mathbf{g}}{g_{\text{ref}}} \tag{10}$$

$$\rho^*=\frac{\rho}{\rho_{ref}};\eta^*=\frac{\eta}{\eta_{\text{ref}}};\sigma^*=\frac{\sigma}{\sigma_{\text{ref}}};\mu^*=\frac{\mu L}{\sigma_{\text{ref}}} \tag{11}$$

where L is the characteristic length scale, U is the reference velocity, the subscript "ref" is for reference values and the superscript "*" stands for dimensionless. The nondimensional governing equations, in which the superscripts "*" are omitted for convenience, are

$$\nabla\cdot\mathbf{u}=0 \tag{12}$$

$$\rho\frac{\partial\mathbf{u}}{\partial t}+\rho\mathbf{u}\cdot\nabla\mathbf{u}=\nabla\cdot\left[-p\mathbf{I}+\frac{1}{\text{Re}}\eta\left(\nabla\mathbf{u}+(\nabla\mathbf{u})^T\right)\right]+\frac{1}{\text{Fr}}\rho\mathbf{g}+\frac{1}{\text{We}}\mu\nabla\phi \tag{13}$$

$$\frac{\partial\phi}{\partial t}+(\mathbf{u}\cdot\nabla)\phi=\frac{1}{\text{We}}\nabla\cdot(M\nabla\mu) \tag{14}$$

where Re is the Reynolds number, We is the Weber number, and Fr is the Froude number. The Ohnesorge number Oh can be obtained from the Reynolds and Weber numbers as follows

$$\text{Re}=\frac{\rho_{ref}UL}{\eta_{ref}};\text{We}=\frac{\rho_{\text{ref}}U^2L}{\sigma_{\text{ref}}};\text{Fr}=\frac{U^2}{g_{\text{ref}}L};\text{Oh}=\frac{\sqrt{\text{We}}}{\text{Re}}=\frac{\eta}{\rho_{\text{ref}}\sigma_{\text{ref}}L} \tag{15}$$

Due to the problem symmetry, the droplet and the substrate can be modeled in a half-domain, as shown in Figure 1, where the droplet falls down from a certain distance above the substrate with an initial velocity. The droplet travels downward due to inertia and gravity, impinges on the rigid horizontal wall and spreads. The boundary conditions are shown in Figure 1, and the equilibrium contact angle between the droplet and the substrate is set to $\pi/2$. Note that the wall boundary is set as no-slip and it requires no special treatment for the moving contact line with the phase-field method because the diffusive interface provides an effective slip length for the contact line to move.[37] To calculate the dimensionless numbers for droplet impact, the droplet diameter D is taken to be the characteristic length scale and the impact velocity U is taken to be the reference velocity. The reference density and viscosity are set to be the density and viscosity of the liquid droplet. The reference surface tension is set to be the surface tension between the liquid and gas phases.

Validation

The model described above has been extensively validated in our previous work against various 1-D analytical models and experiments. The results are presented elsewhere.[38] Here, we only report some representative validation results using a nondimensional version of the model in comparison with experiments reported in literature.[39] Figure 2 shows excellent agreement between the model predictions and experimental data for a water droplet impacting on a steel plate with a contact angle of $\pi/2$, Weber number of 27, and Ohnesorge number of 0.0026. The surrounding medium is air at 20°C and corresponding air density and viscosity are used for the simulation. The tuning factor α needs to be large enough to maintain a constant interface thickness but still low enough not to damp the convection motion. A too high mobility can lead to excessive diffusion of droplets. Here, we set the tuning factor α to the default value 1.

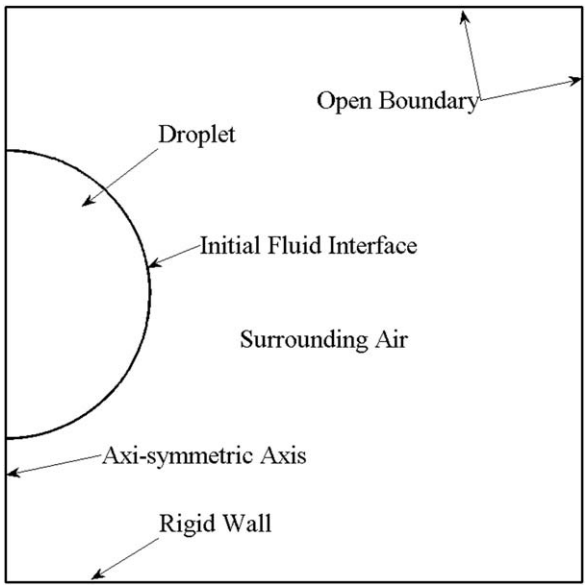

Figure 1. Simulation domain geometry and boundary conditions.

Shape Coefficient Definition

Extensive research has been conducted on shape representation during the past decades for multimedia searching and image retrieval in computer vision, computational geometry, and related fields.[40–42] Various shape descriptors have been proposed to characterize both 2-D and 3-D shapes for multimedia storage, searching, and retrieval. Shape, as a geometric representation of objects in space, contains rich information about the physics of underlying phenomena. Yet, little research has been reported on connecting the shape representation to fundamental understanding of the physical phenomena to support a capability for the model-based rational design and control of complex processes. This section presents an integral metric—a shape coefficient—that we propose to use for characterization of the droplet shape during impact to establish a foundation for side-by-side quantitative comparison of desired and physically realizable shapes.

For a single-droplet impingement, droplet shape can be represented axisymmetrically in 2-D. Methods of 2-D shape representation can be categorized generally into the contour-based and region-based methods.[43] The contour-based method is chosen due to the relatively simple characteristics of droplet shape wherein most of the droplet shape information is contained in the droplet boundary. Because the objective is to achieve a uniform film upon an impact of a single droplet (i.e., to flatten the droplet to a pancake-like structure), the shape metric is defined by measuring the similarity between the actual droplet shape and the desired shape (i.e., a rectangle in 2-D cross-sectional space or a cylinder in 3-D).

To study droplet shape evolution, the droplet image at each time instant can be obtained from the simulation, as

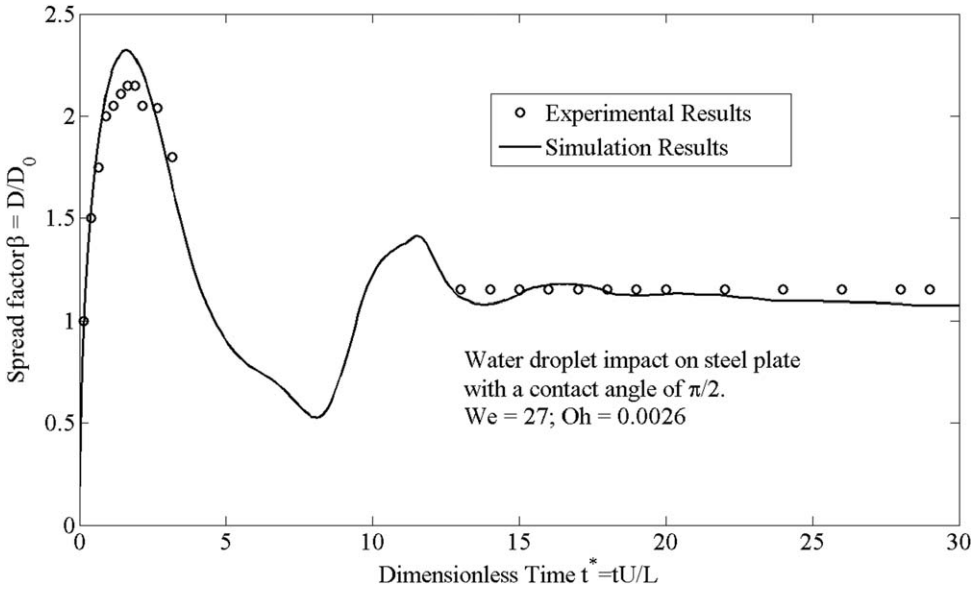

Figure 2. Comparison of experimental data[39] on the spreading radius evolution and simulation results.

representatively shown in Figure 3a. Because the axis of rotation (the left-hand-side edge in Figure 3a is not part of the droplet boundary and, thus, should not be included in the droplet contour, a mirror operation is performed on a half-space droplet representation shown in Figure 3a, resulting in a full droplet cross-section in Figure 3b. The latter contour representation includes only physical interfaces of a droplet projected on a 2-D space which are then processed with a modified Moore-Neighbor tracing algorithm[44] to obtain the droplet contour as shown in Figure 3c.

To define a shape coefficient, we will characterize both the droplet shape and the desired shape with a shape signature function, which will be sampled to give us characteristic vectors for the shapes. The characteristic vectors will be transformed into Fourier domain to filter out high-frequency image noises and facilitate normalization. The shape coefficient will be defined by measuring the Euclidean distance between the characteristic vectors in the Fourier domain. Here, we use the centroid distance as a shape signature.[42] Let the coordinates of the points on the contour obtained from image processing be $(x(j), y(j)$, where $j = 1,2,.N$ and N is the total number of points). We can calculate the centroid of the droplet contour as

$$x_c = \frac{1}{N}\sum_{j=1}^{N} x_j; y_c = \frac{1}{N}\sum_{j=1}^{N} y_j \tag{16}$$

The normalized centroid distance can be defined as

$$r(j) = \sqrt{(x(j)-x_c)^2 + (y(j)-y_c)^2}/D \tag{17}$$

where D is the droplet diameter. Note that the points on the contour acquired from image processing are not evenly distributed and are highly dependent on the specific image and the image processing algorithm and, thus, cannot be directly used to compare the droplet shape from different images. Although Eq. 17 shows that the centroid distance is a function of the coordinates (x, y), a closer look can show that it is a 1-D function that only varies with one independent variable as x and y are related on the contour. A natural choice of the independent variable for the centroid distance would be the polar angle with respect to the centroid. However, during droplet impingement, the droplet shape could sometime be deformed significantly so that the centroid distance changes rapidly with the polar angle. According to Nyquist–Shannon sampling theorem, a very high sampling frequency would be required to obtain sufficient information so that the droplet shape can be recovered from discretely sampled points, which leads to high computational cost and sensitivity to image noises. Therefore, we used the distance d along the contour with respect to a reference point (e.g., the starting point of the contour chosen to be the left bottom corner point) as the independent variable, so that the centroid distance will not change very fast with it no matter what the droplet shape looks like. Then, we can plot the centroid distance of a droplet contour as a function of the normalized distance nd (defined as $d/perimeter$ of the contour) as shown in Figure 4. So a droplet contour can be characterized by the

Figure 3. (a) Half of a droplet cross-section (symmetric about the vertical axis of rotation at the left edge) at one time instant obtained directly from simulation; (b) full cross-section of a droplet by mirror imaging of the half-space image in (a) about the axis of rotation; (c) droplet contour obtained with Moore-Neighbor tracing algorithm.

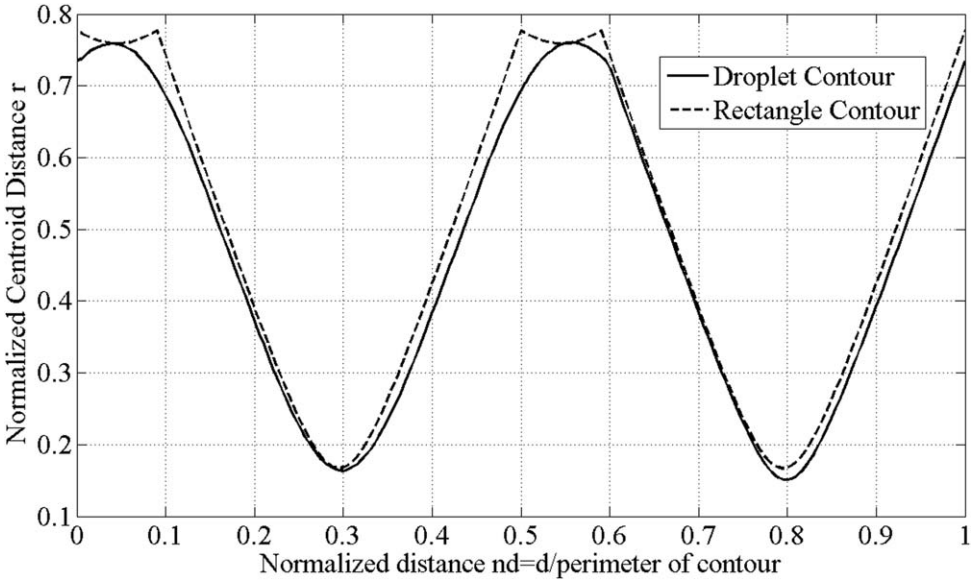

Figure 4. Centroid distance *r* as a function of normalized distance *nd* for droplet contour, rectangle contour.

function *r(nd)*. If a finite number of points is taken on the contour, the characteristic function *r(nd)* becomes a characteristic vector for the droplet shape, which is rotationally and translationally invariant as long as the same reference point is used. The desired geometry is defined as a rectangle that circumscribes the droplet contour as shown in Figure 5, the characteristic function of which is plotted as the dashed line in Figure 4.

Now, measuring the similarity between two shapes becomes computing the "distance" between the two functions defined in the same domain in Figure 4 using one of the possible metrics for the norm of the space. Because the contours are obtained numerically from discrete point image processing, we need to sample these two functions at the same normalized distance to turn these two functions into two vectors, and then measure the distance in the vector space. With the points obtained from image processing algorithm, a piecewise cubic spline is used to fit the shape functions of *r(nd)* and then N_s points are sampled at normalized distance $nd = i/N_s$ (where $i = 0, 1.N_s$) to obtain the characteristic vectors r_d and r_r for the droplet and a desired shape, respectively.

To this point, we developed an approach to measure the similarity between the two shapes in terms of a distance between the two characteristic vectors that parameterize the shape contours. But there are two reasons that we want to take a further step to measure the similarity between the shapes in the frequency domain by taking a Fourier transform of these two vectors. First, if there is a sharp spike somewhere on the droplet contour caused by noise in image processing or acquisition, it can be easily eliminated in the frequency domain using low-pass filtering. Second, if the droplet is scaled differently during the image processing, the characteristic vectors will be scaled, as well as the distance between them, and it is relatively easier to normalize in frequency domain by the direct current (DC) component of the shape due to its averaging characteristics.

Thus, a discrete Fourier transform of the characteristic vectors is computed by Eqs. 18 and 19

$$R_d(k) = \frac{1}{N_s}\sum_{j=1}^{N_S} r_d(j)\exp\left(2\pi i(j-1)(k-1)/N_s\right)/R_d(1) \quad (18)$$

$$R_r(k) = \frac{1}{N_s}\sum_{j=1}^{N_S} r_r(j)\exp\left(2\pi i(j-1)(k-1)/N_s\right)/R_d(1) \quad (19)$$

where R_d and R_r are the Fourier characteristic vectors for droplet and rectangle, respectively, and $R_d(1)$ is the DC component of vector R_d. Normalizing both R_d and R_r by $R_d(1)$ eliminates the baseline scaling effect, but keeps the relative distance between the vectors unchanged. Note that no low-pass filter needs to be applied to eliminate the high-frequency image noises because N_s determines the high cut-off frequency as the fundamental frequency is determined by the length of the signal that is fixed at 1 as shown in Figure 4.

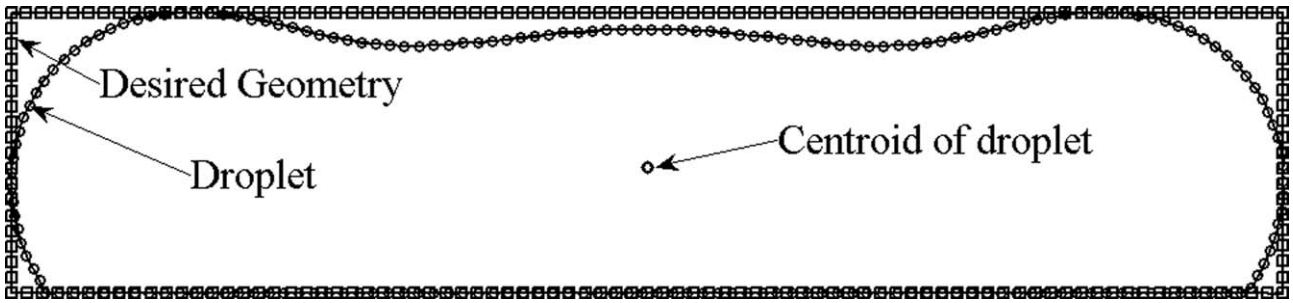

Figure 5. Uniform sampling of droplet contour and the contour of the desired geometry.

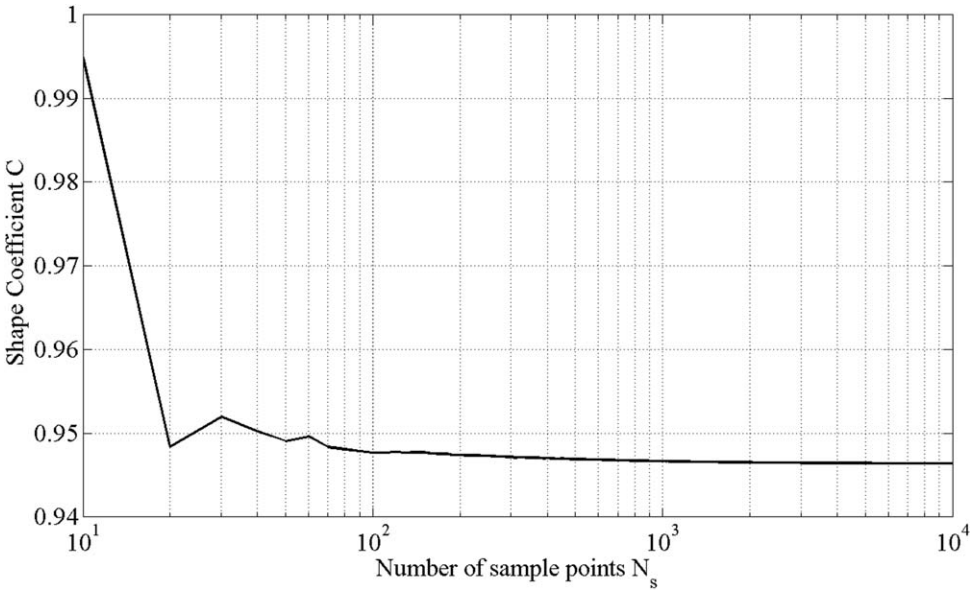

Figure 6. Shape coefficient change with number of sample points.

With the Fourier characteristic vectors, we can, thus, define a shape coefficient to measure the similarity between the simulated or experimentally observed droplet shape and the desired target shape by measuring the Euclidean distance between the two Fourier characteristic vectors

$$C=1-\sqrt{\sum_{j=1}^{N_S}|R_d(j)-R_r(j)|^2}\Big/\sqrt{\sum_{j=1}^{N_S}|R_r(j)|^2} \qquad (20)$$

where R_d and R_r are the Fourier characteristic vectors for the droplet and the desired shape, respectively.

The shape coefficient C ranges from 0 to 1 with unity corresponding to the perfect match between the realized droplet shape and the desired geometry. With this definition of the shape coefficient, we also need to determine how to choose an appropriate N_s, which cannot be too small such that the approximation error is too large and cannot be too large such that the high-frequency noise is introduced. As shown in Figure 6, the shape coefficient converges to a limiting value as N_s increases, and when N_s approaches 200, less than 0.1% relative error is observed for the specific case of droplet shapes considered in this article.

The effectiveness of the shape coefficient in capturing droplet shape upon impact is exemplified in Figure 7. Simulations were performed for the Weber number of 17.9, the Ohnesorge number of 0.085, and the Froude number of 50,968. The shape coefficient, along with the realized and desired (rectangular) droplet shapes at three different time instants, is plotted as a function of time from the moment of impact until the final equilibrium is attained. As one can see from the inset figures, the similarity of droplet shapes is well-captured by maximizing the shape coefficient. The change of the spread factor with time is also plotted for comparison. As we can see, the shape coefficient is able to capture more details of the droplet spreading than the spread

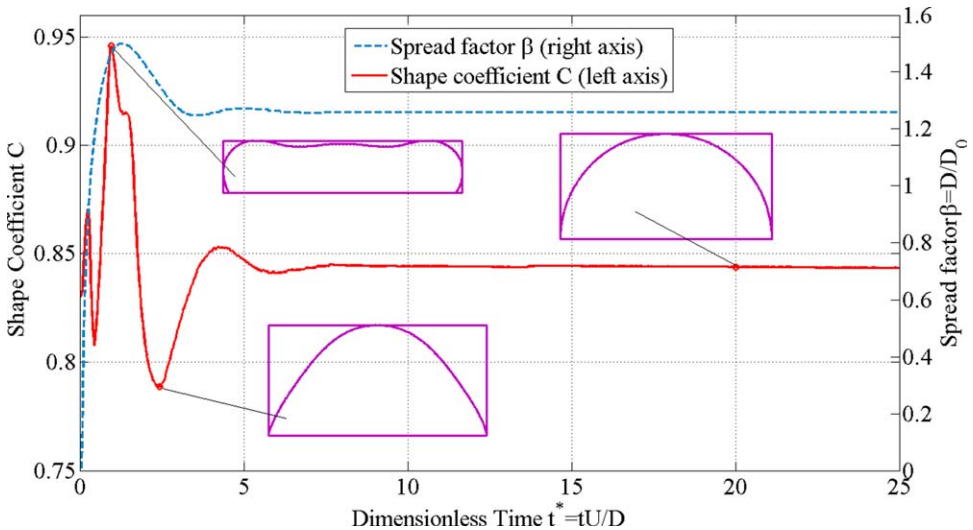

Figure 7. Change of shape coefficient and spread factor with time during the droplet impingement.

[Color figure can be viewed in the online issue, which is available at wileyonlinelibrary.com]

Table 1. Combinations of Weber and Ohnesorge Numbers Used for Simulations

	We = 0.714	We = 17.9	We = 45.7	We = 71.4	We = 121	We = 183
Oh = 0.085	(0.714, 0.085)	(17.9, 0.085)	(45.7, 0.085)	(71.4, 0.085)	(121, 0.085)	(183, 0.085)
Oh = 0.1	(0.714, 0.1)	(17.9, 0.1)	(45.7, 0.1)	(71.4, 0.1)	(121, 0.1)	(183, 0.1)
Oh = 0.129	(0.714, 0.129)	(17.9, 0.129)	(45.7, 0.129)	(71.4, 0.129)	(121, 0.129)	(183, 0.129)
Oh = 0.224	(0.714, 0.224)	(17.9, 0.224)	(45.7, 0.224)	(71.4, 0.224)	(121, 0.224)	(183, 0.224)
Oh = 0.338	(0.714, 0.338)	(17.9, 0.338)	(45.7, 0.338)	(71.4, 0.338)	(121, 0.338)	(183, 0.338)
Oh = 0.4	(0.714, 0.4)	(17.9, 0.4)	(45.7, 0.4)	(71.4, 0.4)	(121, 0.4)	(183, 0.4)

factor. In the early stages of droplet impact, the shape coefficient oscillates significantly, indicating significant changes in droplet shape. However, the spread factor hardly changes and provides much less insight into changes in droplet shape. In addition, the maximum shape coefficient occurs at a different time than the spread factor and usually occurs before the maximum spread factor as shown in Figure 7 and discussed in our previous work.[45] Although this work focuses on shape evolution and attaining an optimal shape upon impact of a single droplet, it would be of significant practical interest to consider a problem of the liquid film shape evolution upon impingement of multiple interacting droplets. Although the physics of interacting droplets will obviously be more complex, the shape coefficient introduced in this article will still be a valid metric to use for assessing the behavior of the deposited liquid layer in respect to its similarity to a desired shape as dictated by the target application.

Results and Discussion

With the defined shape coefficient and the validated numerical model, simulations can be conducted to study the shape evolution of the droplet under different impact conditions. Based on the governing conservation Eqs. 12–15, the impact conditions are determined by the contact angle and three independent dimensionless numbers: Weber number (or Reynolds number), Ohnesorge number, and Froude number. Contact angle is set to $\pi/2$ for this study because the contact angle does not affect the early stage of the droplet spreading much when the spreading is driven by inertial forces.[46] According to previous findings,[45] the Froude number, which represents the relative importance of gravity effects, has little influence on the droplet shape evolution when the droplet diameter is at submillimeter scale, which is of particular interest of our study. Because our objective is to investigate how to optimally flatten a droplet upon impact to produce a uniform thickness pancake-like structure, our primary focus is on studying the effects of the Weber number (or Reynolds number) and the Ohnesorge number on maximizing the achievable shape coefficient and identifying the time instant in the impact sequence that corresponds to the best match between the desired and realized droplet shapes.

A set of simulations is first conducted to study the effects of Weber and Ohnesorge numbers when the Ohnesorge number is small (i.e., much smaller than unity). A 2-D sweep over a range of Weber and Ohnesorge numbers is performed, as shown in Table 1. The droplet diameter is fixed at 50 μm to make the Froude number much larger than corresponding Weber and Reynolds numbers, so that gravity has little influence on the droplet impact results. The results are plotted in Figures 8 and 9.

To explain the results, we need to first take a look at the physics behind the shape evolution of droplet impact. There are three forces that play roles in droplet impact dynamics: the inertia force F_U, the surface tension force F_σ, and the viscous force F_η, which can be defined as

$$F_U = \rho U^2 D^2; F_\sigma = \sigma D; F_\eta = \eta U D \tag{21}$$

During droplet impact, the inertia force drives the fluid to spread and possibly splash, whereas the surface tension force strives to hold the fluid together and viscous force always goes against the moving direction. If there is no surface tension, fluid will try to form a thin film under gravity. If there is no inertia, the surface tension at the liquid-gas, liquid-solid, and solid-gas interfaces will turn the droplet into a spherical cap with an appropriate contact angle, as determined from the Young equation. With this simple insight into droplet behavior in the limiting cases, it is possible to bring some physical meaning to the shape coefficient. The inertial force favors pancake-like shape (corresponding to large shape coefficient), whereas surface tension likes the spherical cap shape (corresponding to small shape coefficient). Because the inertia force corresponds to kinetic energy, surface tension derives from surface energy, and viscous forces dissipate mechanical energy, the energy perspective can be used also to interpret the droplet impact behavior. When the inertia force drives the droplet shape away from the equilibrium spherical cap, kinetic energy is converted to surface energy and when the droplet recoils back to a spherical cap the surface energy is converted to kinetic energy. This kinetic to potential (surface) energy conversion process is dissipative in nature due to the presence of viscous losses. This behavior is similar to oscillation of a simple mechanical spring-mass system, although it is a distributed system.

With the physics in mind, we can explain the results shown in Figures 8 and 9. Because an Ohnesorge number smaller than 1 implies the viscous force is smaller than surface tension, the latter will be the main resistance force that opposes flattening of the droplet shape upon impact. Additionally, the inertia force needs to overcome the surface tension to achieve a flat shape. Therefore, we need the inertia force to be larger than the surface tension (i.e., Weber number is large) for the large shape coefficient to result. In other words, the maximum achievable shape coefficient is primarily influenced by the Weber number, as shown in Figure 8 with little influence of the Ohnesorge number for fluids with relatively low viscosity, and smaller viscous forces as compared to both fluid inertia and surface tension, for which Oh $<<$ 1. However, as the Ohnesorge number is approaching unity, the effect of viscous forces on shape evolution becomes more pronounced (i.e., the curves begin to split in Figure 8) especially in the case when neither surface tension (We $<<$ 1) nor inertia (We $>>$ 1) dominate the shape evolution upon impact. That is when We $\sim$ (1–10) surface tension and inertia balance each other, giving a greater

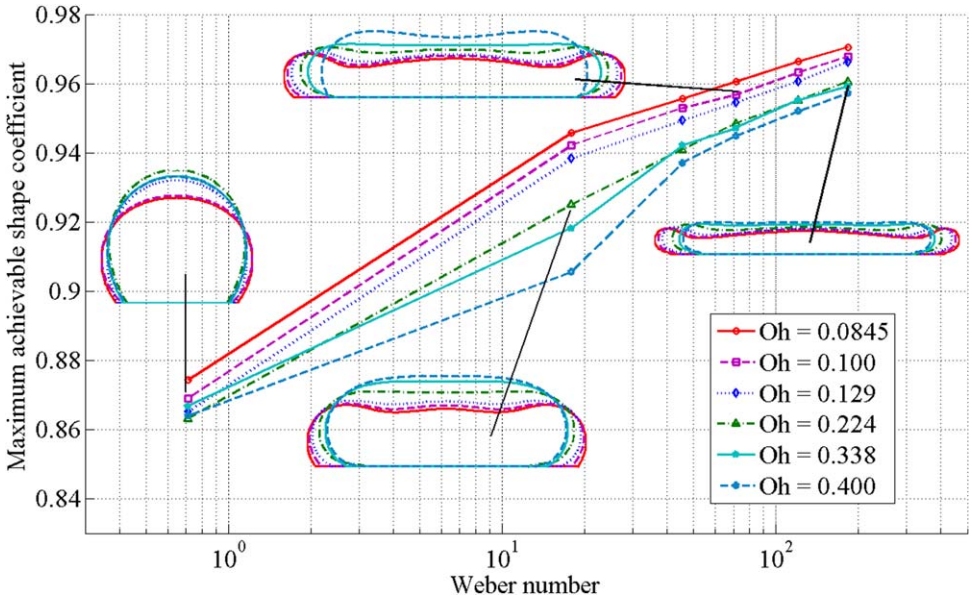

Figure 8. Maximum shape coefficient achieved for varying the Weber number (for low Oh number fluids).

[Color figure can be viewed in the online issue, which is available at wileyonlinelibrary.com]

significance to the viscous stresses in defining how the interface will evolve during the impact. This does not change the overall trend of a monotonic increase in the shape coefficient with the Weber number, but introduces a minor suppression in the rate of this increase as the behavior transitions from surface tension to inertia dominated. In addition, the simulations indicate that when the Ohnesorge number is much smaller than 1 and the Weber number is much larger than 1, the maximum shape coefficient is achieved in the first spreading cycle (i.e., before the droplet reaches its maximum spreading radius); however, when the Ohnesorge number is approaching unity, the maximum shape coefficient does not always occur in the first spreading cycle, especially for the moderately large Weber number cases.[45] It requires either a sufficiently large Weber number, bordering an onset of droplet splash, or a sufficiently small Ohnesorge number for the maximum shape coefficient to occur in the first spreading cycle. When the maximum shape coefficient does occur in the first spreading cycle, we can see from Figure 9 that the Ohnesorge number does not affect much of the dimensionless time (scaled by the inertia time scale) corresponding to the maximum shape coefficient. This is because the viscous forces have minimal effect on the droplet shape evolution during the first spreading cycle when the kinetic energy of the droplet is very high and inertia forces dominate the momentum transport. On the other hand, when droplet inertia is

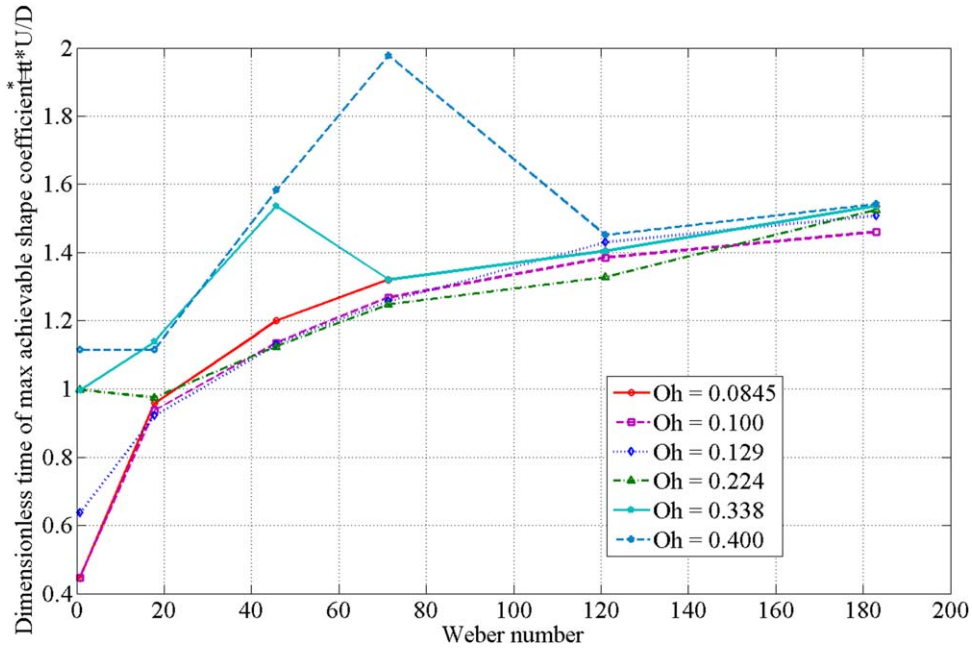

Figure 9. Time instant for achieving a maximum shape coefficient for different Weber numbers (for low Oh number fluids).

[Color figure can be viewed in the online issue, which is available at wileyonlinelibrary.com]

Table 2. Combinations of Reynolds Number and Ohnesorge Number for Simulations

	Re = 0.5	Re = 2.5	Re = 4.0	Re = 5.0	Re = 6.5	Re = 8
Oh = 1.01	(0.5, 1.01)	(2.5, 1.01)	(4, 1.01)	(5, 1.01)	(6.5, 1.01)	(8, 1.01)
Oh = 1.2	(0.5, 1.2)	(2.5,1. 2)	(4, 1.2)	(5, 1.2)	(6.5, 1.2)	(8, 1.2)
Oh = 1.34	(0.5, 1.34)	(2.5, 1.34)	(4, 1.34)	(5, 1.34)	(6.5, 1.34)	(8, 1.34)
Oh = 1.55	(0.5, 1.55)	(2.5, 1.55)	(4, 1.55)	(5, 1.55)	(6.5, 1.55)	(8, 1.55)
Oh = 1.69	(0.5, 1.69)	(2.5, 1.69)	(4, 1.69)	(5, 1.69)	(6.5, 1.69)	(8, 1.69)
Oh = 2	(0.5, 2)	(2.5, 2)	(4, 2)	(5, 2)	(6.5, 2)	(8, 2)
Oh = 2.58	(0.5, 2.58)	(2.5, 2.58)	(4, 2.58)	(5, 2.58)	(6.5, 2.58)	(8, 2.58)
Oh = 4.47	(0.5, 4.47)	(2.5, 4.47)	(4, 4.47)	(5, 4.47)	(6.5, 4.47)	(8, 4.47)
Fr	2.04×10^3	5.09×10^4	1.30×10^5	2.04×10^5	3.45×10^5	5.22×10^5

greater than surface tension, but not overly dominant in the first spreading cycle (i.e., relatively moderate Weber numbers between 10 and 100), the maximum shape coefficient does not necessarily occur in the first spreading cycle as the spreading and shape evolution is defined by the interplay between surface tension and viscous forces.[45] Indeed, this is illustrated by an increased dispersion of the dimensionless time vs. We number curves in Figure 9 as the Ohnesorge number approaches unity. Interestingly, the local maxima are observed in the time required for droplets to reach their maximum shape coefficient, which becomes more pronounced for greater Oh number cases and shifts toward a greater critical We number at which the maximum occurs. The "location" of all maxima corresponds to approximately the same value of the Reynolds number ($Re = We^{1/2}/Oh$) for all cases, which is about 20 for our simulation resolution in terms of the Weber number. This suggests that there is a universal scaling in relative magnitude of inertia and viscous forces that is required to achieve the best match between the physically realized and a desired, pancake-like droplet shape in the case of low-Ohnesorge number fluid droplet impingement.

To assess the effect of the viscous force, rather than surface tension, as a balancing force acting against the fluid inertia upon droplet impact, we performed another set of simulations with viscous force being the main resistance force (i.e., $Oh > 1$). With the hypothesis that the ratio of the inertia force to the main resistance force is the determining factor for shape coefficient, we did a 2-D sweep of Reynolds (instead of the Weber number) and Ohnesorge numbers within the ranges shown in Table 2 (the corresponding Froude numbers for each case are listed in the last row). The results of the simulations are shown in Figures 10 and 11.

As expected, the curves of the maximum achievable shape coefficient with different Ohnesorge numbers collapse together when the Reynolds number is larger than unity as the process is fully dominated by inertia and both the surface tension and viscous force are suppressed. The timing curves shown in Figure 11, depicting a dimensionless time to achieve the maximum shape coefficient, converge to the same value in the limit of small Reynolds number ($Re \sim 1$ and below) and follow the same trend, with some spread but essentially parallel to each other, for larger Reynolds numbers. Note that the definition of the dimensionless time is modified in this case by an additional scaling with the square root of the Weber number to account for the strong effect the surface tension is expected to play in arresting the film spreading when the interface is highly curved near the advancing contact line. Interestingly, when the Reynolds number becomes very large, the dimensionless time to achieve the maximum shape coefficient does not vary significantly.

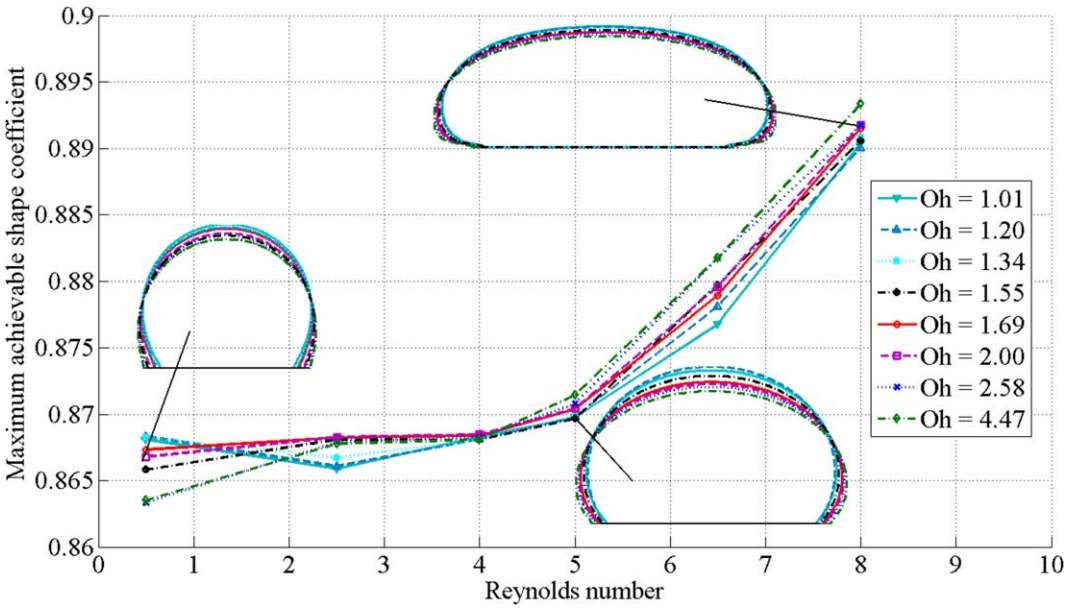

Figure 10. Max shape coefficient achieved for varying the Reynolds number (for high Oh number fluids).

[Color figure can be viewed in the online issue, which is available at wileyonlinelibrary.com]

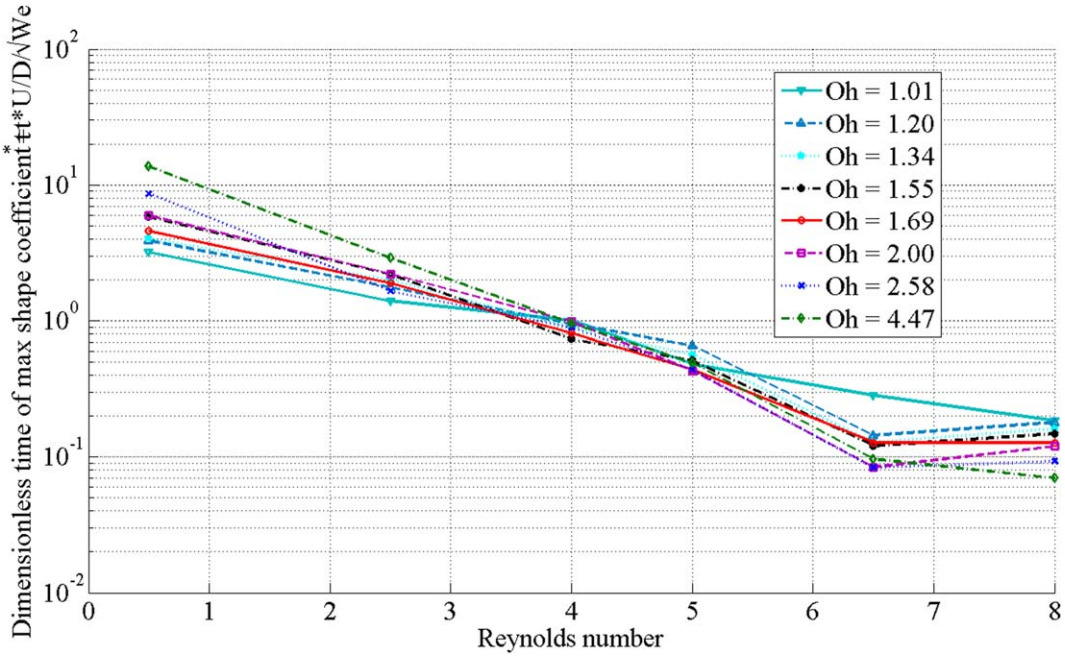

Figure 11. Time instant for achieving a maximum shape coefficient for different Reynolds numbers (for high Oh number fluids).

[Color figure can be viewed in the online issue, which is available at wileyonlinelibrary.com]

Regime Map for Droplet Impact

The results of the analysis presented in Figures 8 through 11 can be placed on a regime map to define the region(s) in the space of relevant dimensionless numbers where we can obtain a desired pancake-like film with a maximum shape coefficient from an impinging droplet on a solid surface. Two equivalent regime maps can be generated with the Ohnesorge number as the abscissa and the Weber or Reynolds number as the ordinate as shown in Figures 12 and 13, respectively. The Ohnesorge number depends only on physical properties and the size of the droplet and, thus, can be viewed as a property variable, whereas the Weber and Reynolds numbers can be viewed as process variables (i.e., they depend on the impingement velocity, which can be controlled regardless of the droplet size and fluid properties). The regime maps are divided into four different domains and typical ranges of maximum achievable shape coefficient and maximum spread factor obtained from simulations in the

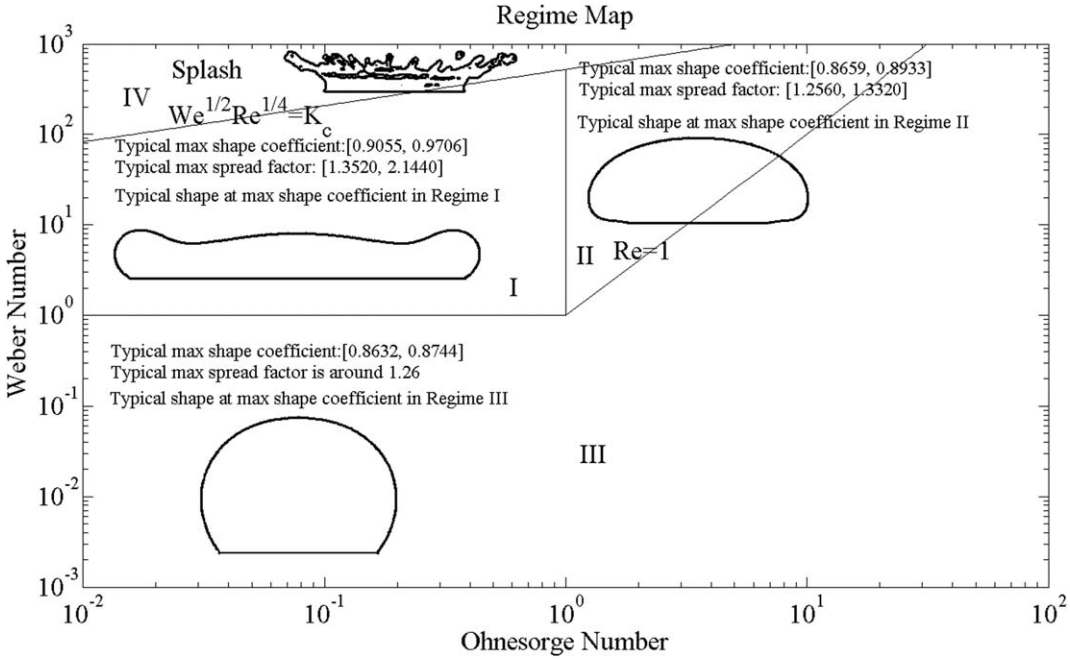

Figure 12. Regime map with Weber number as the ordinate.

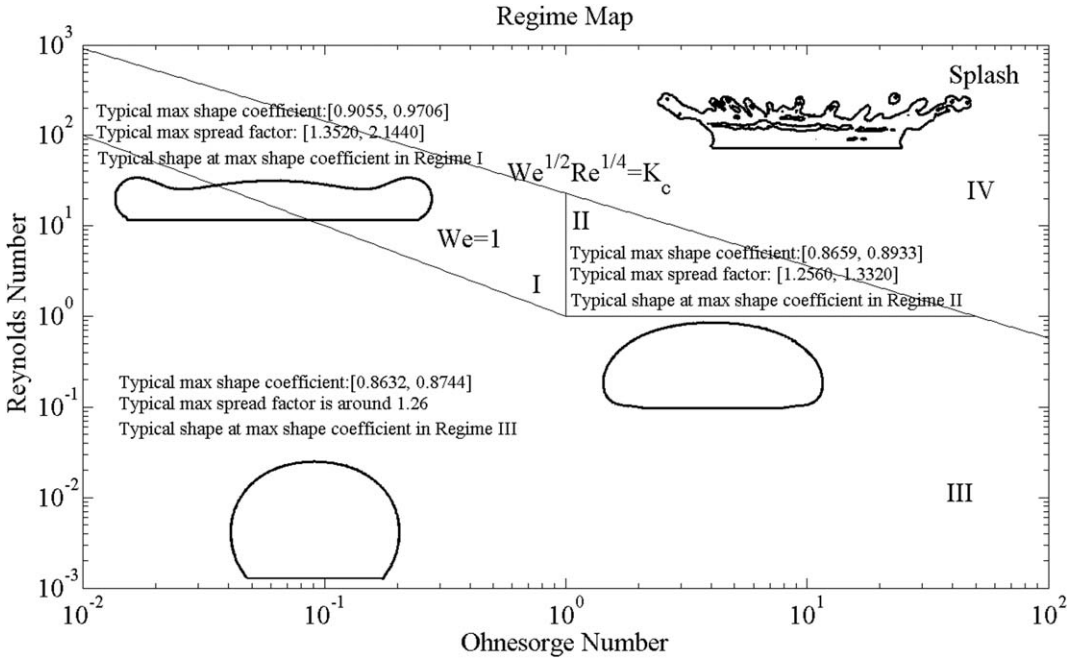

Figure 13. Regime map with Reynolds number as the ordinate.

fourth section are also included. Domains I and II are where the large shape coefficients can be obtained and the droplet shape evolution is dominated by the inertia force. In domain I, the viscous effects are less important and surface tension is the main resistance force; thus, the maximum achievable shape coefficient is mainly determined by the Weber number. The larger the Weber number, the larger shape coefficient can be achieved. Therefore, on the lines that are above and parallel to $We = 1$ (i.e., where $We = const > 1$) in domain I, the maximum shape coefficient does not vary significantly and the time needed to achieve the maximum shape coefficient is also approximately constant. In domain II, the viscous force becomes the main resistance force, as compared to surface tension, and the maximum achievable shape coefficient is mainly controlled by the magnitude of the Reynolds number. That is, the larger the Reynolds number is, the larger shape coefficient can be achieved. On the lines that are above and parallel to $Re = 1$ (i.e., $Re = constant > 1$) in domain II, the maximum achievable shape coefficient stays almost the same regardless of the magnitude of the Ohnesorge number, which is greater than 1 in domain II. The dimensionless time to reach the maximum shape coefficient does depend slightly on the Ohnesorge number, but follows the same trend (see Figure 11) and stops changing after $Re > 10$.

In domain III, the inertia effects are weak and the droplet does not deform much on impact. Its shape evolution is dominated by slow equilibration via the surface tension or viscous forces, depending on the magnitude of the Ohnesorge number. Domain IV is where the inertia is excessively large and splash happens. An empirical relation has been established experimentally to predict when splash happens through the dimensionless number, the "Sommerfeld" parameter $K = We^{1/2}Re^{1/4}$.[17] One can expect splash when K is greater than a critical threshold value of K_c (a reasonable estimate for K_c is $\sim$50 although the exact value of K_c depends on the roughness of the solid surface and the surrounding gas[19]). The surface roughness and surrounding gas effects can be accounted for by choosing an appropriate critical threshold value for K_c which can be obtained empirically in different situations.

It is worth to note that when the Ohnesorge number is greater than K_c, there will never be a chance for the droplet to reach regime II before it splashes as shown in Figure 13. This result is expected because when $Oh > 50$ and $Re > 1$ the surface tension is so weak, as compared to the inertial force, that it cannot hold the droplet together (i.e., a droplet will breakup). That implies that for a highly viscous fluid, a desired pancake-like film topology cannot be realized by a single droplet impact even with sufficiently large impingement speed. Another important observation for applications that one can deduce from the regime II in Figure 13 is that for more viscous fluids (i.e., featuring larger Ohnesorge numbers) there is a smaller limit on the maximum shape coefficient that one can achieve before splash occurs. The conclusion is opposite in regime I (Figure 12), which shows that for more viscous fluids we have a larger upper limit for the maximum achievable shape coefficient.

Conclusions

A numerical model for droplet impact was developed and validated by comparing to experimental data from literature. An integral metric—a shape coefficient—was proposed to provide a quantitative measure of similarity between the physically realized droplet shape and a desired shape, which enabled the study of the shape evolution of droplet impact. The effectiveness of the shape coefficient concept has been tested and it was shown that the shape coefficient was able to find the closest droplet shape to the desired shape during droplet impingement. Simulations were performed to study the effects of the Weber number, Reynolds number, and Ohnesorge number on the maximum achievable shape coefficient. It was found that the maximum achievable shape coefficient was mainly determined by the Weber number when the Ohnesorge number is smaller than 1, and increasing the

Weber number results in a larger shape coefficient. It has also been found that the Reynolds number is the main determining factor of the maximum achievable shape coefficient when Ohnesorge number is greater than 1. The physics behind the droplet impact was examined and used to explain the results. Using an insight obtained from parametric simulations of the limiting cases, a regime map was developed to indicate the domains in the space of relevant dimensionless parameters where a desired pancake-like droplet shape can be obtained upon impact while avoiding a detrimental effect of splash. Important implications were derived on the processing conditions for practical applications involving drop-on-demand thin film deposition of high viscosity fluids with high degree of thickness uniformity through critical analysis of the impingement regime maps.

Acknowledgments

The authors acknowledge the U.S. National Science Foundation, through award DMI-0900322. Any opinions, findings, and conclusions or recommendations expressed in this publication are those of the authors and do not necessarily reflect the views of the National Science Foundation.

Literature Cited

1. Worthington AM. On the forms assumed by drops of liquids falling vertically on a horizontal plate. *Proc R Soc Lond*. 1876;25:261–271.
2. Rein M. Phenornena of liquid drop impact on solid and liquid surfaces. *Fluid Dyn Res*. 1993;12:61–93.
3. Chandra S, Avedisian CT. On the collision of a droplet with a solid surface. Proceedings: Mathematical and Physical Sciences. London, 1991;13–41.
4. Zhao Z, Poulikakos D, Fukai J. Heat transfer and fluid dynamics during the collision of a liquid droplet on a substrate-II. *Int J Heat Mass Transf*. 1996;39:2791–2802.
5. Kim HY, Chun JH. The recoiling of liquid droplets upon collision with solid surface. *Phys Fluids*. 2001;13:643–659.
6. Šikalo Š, Tropea C, Ganić EN. Impact of droplets onto inclined surfaces. *J Colloid Interface Sci*. 2005;286:661–669.
7. Perelaer J, Smith PJ, van den Bosch E, van Grootel SSC, Ketelaars PHJM, Schubert US. The spreading of inkjet-printed droplets with varying polymer molar mass on a dry solid substrate. *Macromol Chem Phys*. 2009;210:495–502.
8. Son Y, Kim C, Yang DH, Ahn DJ. Spreading of an inkjet droplet on a solid surface with a controlled contact angle at low weber and reynolds numbers. *Langmuir*. 2008;24:2900–2907.
9. Léopoldès J, Dupuis A, Bucknall DG, Yeomans JM. Jetting micron-scale droplets onto chemically heterogeneous surfaces. *Langmuir*. 2003;19:9818–9822.
10. Rioboo R, Marengo M, Tropea C. Time evolution of liquid drop impact onto solid, dry surfaces. *Exp Fluids*. 2002;33:112–124.
11. Schiaffino S, Sonin AA. Molten droplet deposition and solidification at low Weber numbers. *Phys Fluids*. 1997;9:3172–3187.
12. Dussan EB. On the spreading of liquids on solid surfaces: static and dynamic contact lines. *Annu Rev Fluid Mech*. 1979;11:371–400.
13. Carey VP. Liquid-Vapor Phase Change Phenomena, an Introduction of Vaporization and Condensation Processes in Heat Transfer Equipment. Washington: Hemisphere Publishing Corporation; 1992.
14. Lee J, Kim J, Kiger KT. Time- and space-resolved heat transfer characteristics of single droplet cooling using microscale heater arrays. *Int J Heat Mass Transfer*. 2001;22:188–200.
15. Nagai N, Carey VP. Assessment of surface wettability and its relation to boiling phenomena. *Thermal science and engineering*. 2002;10:1–9.
16. Stow CD, Hadfield MG. An experimental investigation of fluid flow resulting from the impact of a water drop with an unyielding dry surface. Proceedings of the Royal Society of London. A. Mathematical and Physical Sciences, 1981;373:419–441.
17. Mundo C, Sommerfeld M, Tropea C. Droplet-wall collisions - experimental studies of the deformation and breakup process. *Int J Multiphas Flow*. 1995;21:151–173.
18. Xu L, Zhang WW, Nagel SR. Drop splashing on a dry smooth surface. *Phys Rev Lett*. 2005;94:184505.
19. Xu L, Barcos L, Nagel SR. Splashing of liquids: interplay of surface roughness with surrounding gas. *Phys Rev E*. 2007;76:066311.
20. Range K, Feuillebois F. Influence of surface roughness on liquid drop impact. *J Colloid Interface Sci*. 1998;203:16–30.
21. Pepper RE, Courbin L, Stone HA. Splashing on elastic membranes: the importance of early-time dynamics. *Phys Fluids*. 2008;20:082103.
22. McHale G, Rowan SM, Newton MI. Frenkel's method and the spreading of small sperical droplets. *J Phys D*. 1994;27:2619.
23. Bechtel SE, Bogy DB, Talke FE. Impact of a liquid drop against a flat surface. *IBM J Res Dev*. 1981;25:963–971.
24. Asai A, Shioya M, Hirasawa S, Okazaki T. Impact of an ink drop on paper. *J Imaging Sci Technol*. 1993;37:205–207.
25. Scheller BL, Bousfield DW. Newtonian drop impact with a solid surface. *AIChE J*. 1995;41:1357–1367.
26. Mao T, Kuhn DCS, Tran H. Spread and rebound of liquid droplets upon impact on flat surfaces. *AIChE J*. 1997;43:2169–2179.
27. Attané P, Girard F, Morin V. An energy balance approach of the dynamics of drop impact on a solid surface. *Phys Fluids*. 2007;19:012101 (012101-1 to 012101-17).
28. Harlow FH, Welch JE. Numerical calculation of time dependent viscous incompressible flow of fluid with free surface. *Phys Fluids*. 1965;8:2182–2189.
29. Sussman M, Smereka P, Osher S. A level set approach for computing solutions to incompressible two-phase flow. *J Comput Phys*. 1994;114:146–159.
30. Juric D, Tryggvason G. A front-tracking method for dendritic solidification. *J Comput Phys*. 1996;123:127–148.
31. Jacqmin D. Calculation of two-phase navier-stokes flows using the phase-field modeling. *J Comput Phys*. 1999;155:96–127.
32. Bussmann M, Mostaghimi J, Chandra S. On a three-dimensional volume tracking model of droplet impact. *Phys Fluids*. 1999;11:1406–1417.
33. Schwartz LW, Eley RR. Simulation of droplet motion on low-energy and heterogeneous surfaces. *J Colloid Interface Sci*. 1998;202:173–188.
34. Lee T, Liu L. Lattice Boltzmann simulations of micron-scale drop impact on dry surfaces. *J Comput Phys*. 2010;229:8045–8063.
35. Cahn JW, Hilliard JE. Free energy of a nonuniform system. I. Interfacial free energy. *J Chem Phys*. 1958;28:258–267.
36. Yue P, Zhou C, Feng JJ, Ollivier-Gooch CF, Hu HH. Phase-field simulations of interfacial dynamics in viscoelastic fluids using finite elements with adaptive meshing. *J Comput Phys*. 2006;219:47–67.
37. Jacqmin D. Contact-line dynamics of a diffuse fluid interface. *J Fluid Mech*. 2000;402:57–88.
38. Zhou W, Loney D, Fedorov AG, Degertekin FL, Rosen DW. Impact Of Polyurethane Droplets on a Rigid Surface for Ink-Jet Printing. 21st International Solid Freeform Fabrication Symposium, Austin, TX, August 9–11, 2010:524–538.
39. Pasandideh-Fard M, Qiao YM, Chandra S, Mostaghimi J. Capillary effects during droplet impact on a solid surface. *Phys Fluids*. 1996;8:650–659.
40. Arbter K, Snyder WE, Burhardt H, Hirzinger G. Application of affine-invariant fourier descriptors to recognition of 3-D Objects. *IEEE Trans Pattern Anal Mach Intell*. 1990;12:640–647.
41. Zhang D, Lu G. A comparative study on shape retrieval using fourier descriptors with different shape signatures. *J Vis Commun Image Represent*. 2003;14:41–60.
42. Davies ER. Machine Vision: Theory, Algorithms, Practicalities, 3rd Ed. Burlington, MA: Morgan Kaufmann, 2005.
43. Zhang D, Lu G. Review of shape representation and description techniques. *Pattern Recognit*. 2004;37:1–19.
44. Pavlidis T. Algorithms for Graphics and Image Processing. Rockville, MD: Computer Science Press; 1982.
45. Zhou W, Loney D, Fedorov AG, Degertekin FL, Rosen DW. Droplet impingement dynamics in ink-jet deposition. *Virtual Phys Prototy*. 2012;7:49–64.
46. Dong H, Carr WW, Bucknall DG. Temporally-resolved inkjet drop impaction on surfaces. *AlChE J*. 2007;53:2606–2617.

Manuscript received Aug. 27, 2012, and revision received Jan. 17, 2013.